Scripta Materialia 252 (2024) 116239

Contents lists available at ScienceDirect

Scripta Materialia

journal homepage: www.journals.elsevier.com/scripta-materialia

Low-fatigue large elastocaloric effect in NiTi shape memory alloy enabled by two-step transition

Qianglong Liang [a,*], Dong Wang [b], Chuanxin Liang [b], Xiangdong Ding [a,*], Yunzhi Wang [c]

[a] State Key Laboratory for Mechanical Behavior of Materials, Xi'an Jiaotong University, Xi'an, Shaanxi 710049, China
[b] Center of Microstructure Science, Frontier Institute of Science and Technology, State Key Laboratory for Mechanical Behavior of Materials, Xi'an Jiaotong University, Xi'an, Shaanxi 710049, China
[c] Department of Materials Science and Engineering, The Ohio State University, 2041 College Road, Columbus, OH 43210, USA

ARTICLE INFO

Keywords:
Martensitic transformation
Elastocaloric effect
Shape memory alloy
NiTi

ABSTRACT

NiTi shape memory alloys are promising elastocaloric materials owing to their substantial adiabatic temperature change (ΔT_{ad}). However, the simultaneous attainment of large ΔT_{ad} and low fatigue poses challenges due to the significant hysteresis and severe functional fatigue associated with the autocatalytic avalanche-like martensitic transformation. This study demonstrates a continuous two-step transition in $Ni_{50.8}Ti_{49.2}$ (at.%), showcasing cyclic-stable superelasticity with large recoverable strain (5.9 %), substantial ΔT_{ad} (19.1 K) and high coefficient of performance. *In-situ* loading analysis indicates a stress-induced continuous transition from the B2 to R and subsequently to B19′. Nanoscale lattice analysis exposes heterogeneous strain network, harboring metastable R phase preceding the B19′ phase. By exploiting differences in critical stress and transformation potential between R and B19′ phases, this study demonstrates the possibilities to synergistically integrate functional performances of different martensitic phases in NiTi into a sequential and continuous two-step transition to provide controlled strain release with unprecedented properties.

Vapor compression cooling, prevalent in refrigeration technology, faces efficiency limit and, more importantly, environmental concerns like greenhouse gas emissions and toxic refrigerants [1,2]. Solid-state cooling, employing caloric materials and leveraging field-induced temperature changes during reversible phase transitions, emerges as an alternative [3,4]. Martensitic transformations (MTs) induced by temperature or stress in shape memory alloys (SMAs) are accompanied by heat absorption and elastocaloric effects [5]. By applying mechanical stress or strain, the elastocaloric effect in SMAs provides an alternative to vapor compression cooling with high energy conversion efficiency [6,7]. NiTi, a widely used SMA, exhibits a noteworthy adiabatic temperature change (ΔT_{ad}) of up to 35 K [8], making it a promising elastocaloric cooling material. However, thermomechanical hysteresis and severe functional fatigue in NiTi SMAs hinder energy efficiency and long-term service in practical refrigeration applications.

The conventional autocatalytic and avalanche-like B2 to B19′ MT in NiTi SMAs generates structural defects, including dislocations and subgrain boundaries [9-14], leading to degradation of mechanical and functional properties during transformation cycling. Various strategies, such as lattice compatibility, precipitation (Ti_3Ni_4, Ti_2Cu), grain refinement, and composites (TiNi/$TiNi_3$, crystalline/amorphous), have been employed to mitigate the violent MT behavior and improve fatigue resistance in NiTi-based SMAs [15-24]. Although many efforts convert the plateau-shaped superelastic stress-strain behavior into quasi-linear superelasticity with slim hysteresis and high fatigue resistance, these approaches often compromise the overall transformability of the system, resulting in small recoverable strain and limited elastocaloric ΔT_{ad} as compared to the conventional NiTi SMAs [18-24]. For example, the introduction of coherent $TiNi_3$ and Ti_2Ni_3 precipitates with a heterogeneous microstructural design extends the fatigue life of bulk NiTi SMAs to millions of cycles, yet high-density intermetallic phases reduce the output elastocaloric ΔT_{ad} down to 4∼6 K with superelastic recoverable strain less than 3 % [23,24]. Recent investigations on cyclic-stable quasi-linear superelasticity by transforming autocatalytic MT into a highly reversible strain glass transition under local strain field network achieved through cold work of conventional superelastic NiTi SMA [25-27] show great promise on mitigating the functional fatigue problem. However, the pronounced structural confinement inherent in strain glasses imposes limitations on the overall work output and energy conversion efficiency, and increases significantly the stimulus stress

* Corresponding authors at: State Key Laboratory for Mechanical Behavior of Materials, Xi'an Jiaotong University, Xi'an, Shaanxi 710049, China.
E-mail addresses: liangqianglong@xjtu.edu.cn (Q. Liang), dingxd@xjtu.edu.cn (X. Ding).

https://doi.org/10.1016/j.scriptamat.2024.116239
Received 29 March 2024; Received in revised form 12 May 2024; Accepted 14 June 2024
Available online 20 June 2024
1359-6462/© 2024 Acta Materialia Inc. Published by Elsevier Ltd. All rights are reserved, including those for text and data mining, AI training, and similar technologies.

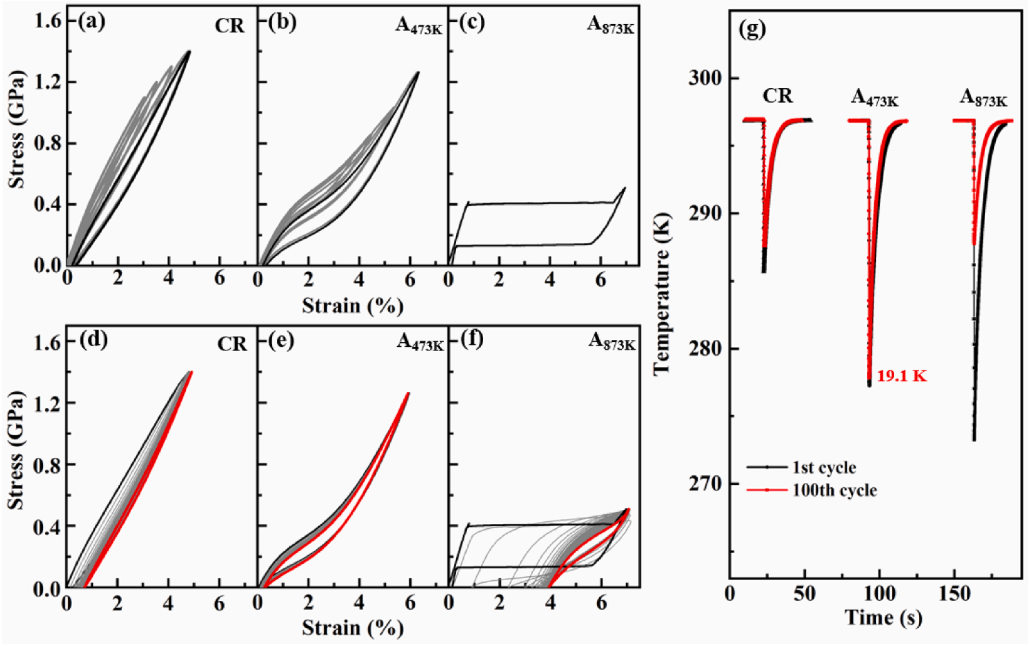

Fig. 1. Superelastic and elastocaloric properties of $TiNi_{50.8}$ alloy under cold-rolling and different annealing treatments. (a-c) Pre-tensile tests to obtain the maximum recoverable strain of different sample. (d-f) Strain-stress loops measured by cyclic loading for 100 cycles with the first cycle in black, the last cycle in red and rest in grey. (g) Elastocaloric measurement of ΔT_{ad} for the first and last cycles.

[28]. For instance, the strain glass transition in severely cold-worked $Ni_{50.6}Ti_{49.4}$ exhibits a diminished ΔT_{ad} of 5.5 K [29].

Drawing inspiration from the strategies enhancing electrostrain in relaxor ferroelectrics through the introduction of different ferroelectric phases with varying local polarizations [30,31], we propose a sequential transition pathway between distinct martensitic states with varying local strains to augment recoverable strain and thereby increase ΔT_{ad}. Incorporating an intermediate transition state, featuring a lower energy barrier between different martensitic states, has the potential to enhance superelastic recoverable strain. This is facilitated by the easier transformation and growth of local martensitic domains across various martensitic phases, promising an improved elastocaloric response. The minimal hysteresis observed in continuous transitions leads to decreased energy dissipation during stress-induced transition cycles, suggesting that a multi-stage strain glass transition could enhance the elastocaloric coefficient of performance (COP) [28].

To investigate the hypothesis, a slightly Ni-rich NiTi SMA, $Ni_{50.8}Ti_{49.2}$ (at.%) is used in this work, known to undergo B2-R-B19′ MTs under thermomechanical treatments [32]. The solutionized specimens are cold-rolled to 40 % thickness reduction, and then annealed at different temperatures (873 K and 473 K) for 2 h flowing water quench to room temperature, denoted as CR, A_{473K}, and A_{873K} in this work. For mechanical testing, dog-bone specimens are prepared and subjected to tensile tests using an Instron 5969 universal test machine at a loading-unloading strain rate of 10^{-3} s^{-1}. Strain is recorded using a video extensometer with a 10 mm gauge length. Prior to cyclic loading tests and elastocaloric measurements, specimens are pre-tensile loaded to the maximum recoverable strain. After holding the sample at maximum strain to reach equilibrium room temperature, elastocaloric effects are evaluated through rapid unloading at a strain rate of 0.2 s^{-1} to maintain adiabatic conditions, with ΔT_{ad} measured by a T-type thermoelectric couple. Differential scanning calorimetry (DSC) measurements are conducted using a TA Q200 instrument with a cooling and heating rate of 10 K min^{-1} to analyze heat flow curves and transformation latent heat. Foils for transmission electron microscopic observations are prepared using twin jet electropolishing with an electrolyte comprising 20 % H_2SO_4 and 80 % CH_3OH (vol.%) at 253 K. High-angle annular dark-field imaging (HAADF) is performed using a ThermoFisher Talos-F20 scanning/transmission electron microscope (S/TEM) operating at 200 kV with a field-emission gun. In-situ loading synchrotron-based high--energy X-ray diffraction (HE-XRD) experiments are conducted at beamline 11-ID-C of the Advanced Photon Source at Argonne National Laboratory. A monochromatic X-ray beam with a wavelength of 0.1173 Å and a size of 500 × 500 μm is utilized to monitor volume fraction changes during in-situ loading. DigitalMicrograph software (version 3.43.3213.0) is used for fast Fourier transformation (FFT) processing. Geometric phase analysis (GPA) is used to measure the strain field from atomic HAADF image [33]. In the $[100]_{B2}$ zone orientation, the $(011)_{B2}$ reflections in the FFT pattern were used for GPA.

To assess and compare the superelastic and elastocaloric properties, cyclic tensile tests are conducted on CR, A_{473K}, and A_{873K} samples are measured spanning 100 cycles. Before the cyclic tests, due to the distinctive slim stress-strain loop characteristic, CR and A_{473K} samples undergo pre-tensile loading under progressively increased strain and stress to assess the potential maximum recoverability, as shown in Fig. 1 (a-b). In contrast, the A_{873K} sample, which exhibits a plateau-like superelastic behavior indicative of conventional martensitic transformation, is directly tensile loaded to the end of stress plateau to obtain the maximum superelasticity without the training process under increased applying strain, as shown in Fig. 1(c). Fig. 1(d-f) illustrate the following 100 stress-strain cyclic tensile loops, with the first cycle depicted in black, the last in red, and intermediary cycles in grey for clarity. Elastocaloric ΔT_{ad} values for the first and last cycles of these samples are presented in Fig. 1(g). CR samples, known to undergo a B19′ strain glass transition [25], exhibit quasi-linear superelasticity with high strength. Conversely, A_{473K} samples display non-linear superelasticity from the outset, characterized by modulus softening and slim stress-strain hysteresis loops, with no significant degradation observed over subsequent cycles. A_{873K} samples, representing well-annealed specimens with B19′ MT [34], demonstrate typical stress-induced MT (SIMT) behavior, featuring a stress plateau and large stress-strain hysteresis. Although A_{873K} samples initially exhibit very large recoverable strain and elastocaloric ΔT_{ad}, these properties were significantly reduced after cyclic testing due to functional fatigue. Superior cyclic stability is observed in the CR and A_{473K} samples, with no evident degradation in ΔT_{ad} after cyclic testing for both. Furthermore, A_{473K}

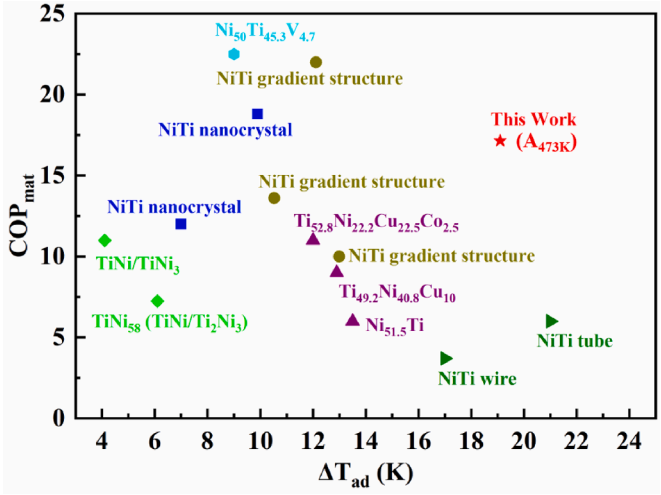

Fig. 2. Comparisons of the elastocaloric property. The elastocaloric performance of COP_{mat} and ΔT_{ad} of A_{473K} sample are compared with various NiTi-based elastocaloric materials, including conventional NiTi wires and tubes [36,37], nanocrystalline NiTi tubes and cylinders [21,38], nanocomposite (TiNi/$TiNi_3$, TiNi/Ti_2Ni_3) [23,24], gradient structured NiTi [39-41], precipitated NiTi [20,42,43], and NiTi-based SMA with lattice compatibility ($Ni_{50}Ti_{45.3}V_{4.7}$) [44].

samples display much larger superelastic recoverable strain (5.9 %) and ΔT_{ad} (19.1 K) compared to CR samples while maintaining cyclic stability. This behavior deviates from both conventional MT, characterized by large recoverable strains but highly non-linear superelasticity with stress plateaus and severe functional fatigue, and strain glass transitions, characterized by quasi-linear superelasticity with slim hysteresis and small recoverable strains. The elastocaloric COP of material (COP_{mat}) of the A_{473K} samples is then determined by $COP_{mat} = \Delta Q/\Delta W = \rho C_p \Delta T_{ad}/\Delta W$, where ΔQ, ρ, C_p, ΔT_{ad}, and ΔW represent the cooling capacity, density, specific heat capacity, adiabatic temperature drop, and the stress-strain hysteresis loop area, respectively [35]. The COP_{mat} and ΔT_{ad} of A_{473K} sample are then plotted in Fig. 2 under a direct comparison to the summarization of values in literature of various NiTi-based elastocaloric materials obtained under similar adiabatic unloading condition to maintain comparability [20,21,23,24,36-44], which highlight the exceptional performance of the A_{473K} sample.

To delve into the transition behavior underlying superelastic and elastocaloric properties, heat flow curves of different samples are measured and depicted in Fig. 3(a-c) during cooling and heating within the temperature range of 375 K to 125 K. In Fig. 3(a-b), both exothermic and endothermic peaks are absent in the CR and A_{473K} samples, contrasting with the conventional MT behavior observed in the A_{873K} well annealed samples in Fig. 3(c). Similar to the CR sample previously identified as displaying strain glass transition [25,26], the A_{473K} samples are anticipated to exhibit a similar continuous transition, triggering the detected cyclic-stable superelastic behavior.

To establish a direct link between the stress-induced transition and the functional properties, *in-situ* loading synchrotron-based HE-XRD analysis is conducted at room temperature. Only B2-phase peaks are clearly visible without loading in Fig. 4(a). Three isolated diffraction peaks corresponding to $(112)_{B2}$, $(113)_R$ and $(001)_{B19'}$ are presented in Fig. 4(b) to show direct comparison under applied stress. Upon loading from 0 to 500 MPa, the intensity of the $(112)_{B2}$ peak gradually decreases, while the $(113)_R$ peak initially increases and then decreases. Simultaneously, the $(001)_{B19'}$peak continues to increase during the decrease of the $(113)_R$ peak. Additionally, a slight shift in the peak positions of all the revealed peaks is observed under the applied stress. The relative volume fraction changes of the B2, R and B19′ phases are determined by comparing the integrated peak intensities under the applied stress, as shown in Fig. 4(c). The volume fraction indicates an initial continuous growth of the R phase, reaching a maximum near 350 MPa, followed by the growth of the B19′ phase at the expense of both the B2 and R phases. To evaluate the lattice elastic strain evolution during the stress-induced B2→R→B19′ transition, the *d*-spacing of the peaks under stress is compared to their initial values. This yield lattice strain $\varepsilon_{hkl} = 100\ \% \times (d_{hkl} - d_0)/d_0$, where d_{hkl} and d_0 are the interplanar spacing of the (hkl) planes with and without the external stress. Fig. 4(d) illustrates the changes in lattice strain for the B2, R and B19′ phases as a function of the applied strain. The results indicate that the lattice strain of the B2 phase responds rapidly to the applied strain. In contrast, the lattice strain of the R phase exhibits only a limited increase with a plateau after the decrease in volume fraction. The lattice strain of the B19′ phase shows a strong correlation with the volume fraction, exhibiting a slow increase during the R phase transition followed by increase during the B19′ transition.

It should be noted that the stress-induced continuous transition behavior observed in our current work diverges from the conventional martensitic transformations typically detected by DSC. In conventional NiTi SMAs, such transformations, exemplified by the A_{873K} sample in Fig. 1, are characterized by stress plateaus accompanied by significant stress-strain hysteresis and functional fatigue [45], readily detectable by DSC during cooling and heating cycles, as illustrated in Fig. 3. The absence of detectable martensitic transformations by DSC in our study does not negate the presence of a unique stress-induced continuous transition mechanism. This mechanism, evidenced by the sequential transition from the B2 phase to the R phase and subsequently to the B19′ phase under external loading, is indicative of a distinct mechanical response not governed by conventional thermal or stress-induced

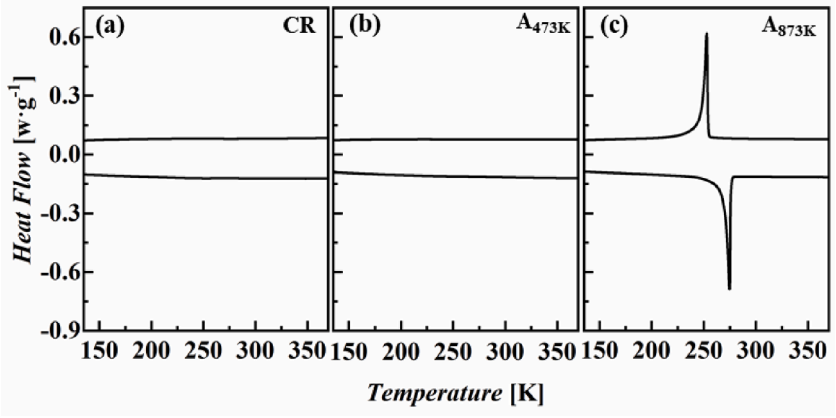

Fig. 3. DSC transition behavior measurements of the $TiNi_{50.8}$ SMA under cold rolling and different annealing conditions. (a-c) DSC heat flow loops upon cooling and heating of the CR, A_{473K}, and A_{873K} samples.

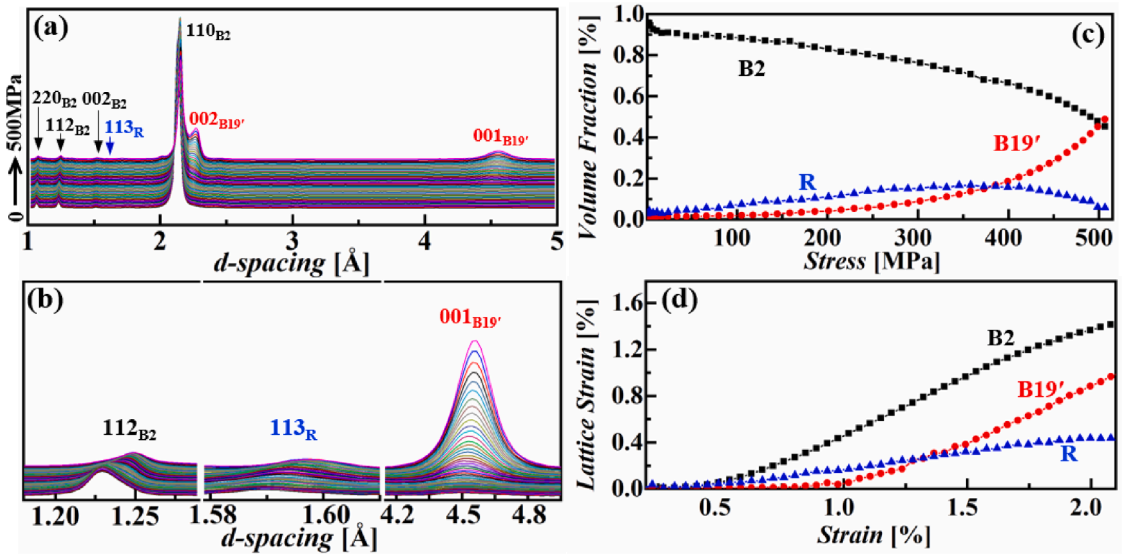

Fig. 4. *In-situ* loading synchrotron-based HE-XRD analysis of stress-induced transition behavior. (a) Diffraction profile upon loading. (b) Isolated peaks in the diffraction profile corresponding to $(112)_{B2}$, $(113)_R$, and $(001)_{B19'}$ plotted in relation to tensile stress. (c-d) The volume fraction and lattice strain of B2, R and B19′ under loading evaluated in relation to stress and strain, illustrating the stress-induced B2→R→B19′ TSGT behavior. The stress and stain are correlated in (c) and (d).

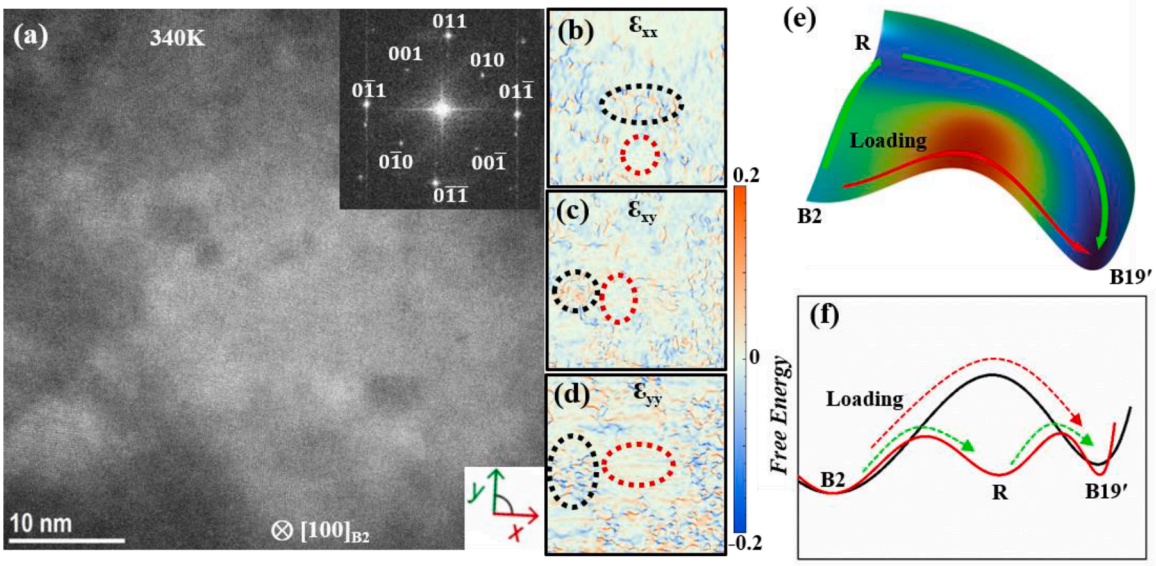

Fig. 5. Nanoscale heterogeneous strain field underlying two-step transition pathway. (a) HAADF image of B2 parent phase in $[100]_{B2}$ zone axis. FFT reflections corresponding to HAADF image is shown in the inset of (a). (b-d) lattice strain maps (ε_{xx}, ε_{xy}, ε_{yy}) obtained based on the lattice image in (a) by GPA. The heterogenous lattice strain map is depicted, showing areas with low and high lattice distortions indicated by black and red dashed circles. (e-f) Free-energy landscape under external loading of the stress-induced B2→R→B19′ transition pathway in comparison to the B2→B19′ pathway with much smaller energy barrier.

martensitic transformations. Our previous investigations [24-26], have similarly demonstrated the prevalence of continuous transition behavior under external loading in NiTi SMAs, even in samples where conventional martensitic transformations are not detected by DSC. Therefore, the confinement of conventional martensitic transformations is instrumental in facilitating the superior cyclic stability and enhanced mechanical properties observed in our study, wherein stress-induced continuous transitions predominate under external loading conditions. This B2→R→ B19′ continuous transition pathway directly contributes to the measured cyclic-stable non-linear slim superelasticity.

Nano-scale lattice strain analysis is conducted to elucidate the origin of the stress-induced two-step continuous transition pathway through atomic STEM-HAADF observation. An HAADF image capturing nano-scale lattice distortions in the $[100]_{B2}$ zone axis is obtained at 340 K, as shown in Fig. 5(a). The elevated temperature is used for HAADF observation to avoid the precursor phenomenon in the $TiNi_{50.8}$ (at.%) generated by the external Ni content as point defect, which may produce R-like nanodomain structure hindering the accurate evaluation of local lattice strain in the B2 matrix [46,47]. The corresponding FFT reflections exclusively reveal the B2 parent phase. Utilizing geometrical phase analysis (GPA) [33], lattice strain maps (ε_{xx}, ε_{xy}, ε_{yy}) corresponding to the HAADF image are obtained. The strain maps in Fig. 5 (b-d) reveal a heterogeneous spatial distribution of lattice strain, with peak values above 10 %. Previous research has suggested that different martensitic phases can be guided into a continuous transition by nano-scale local lattice strain field [46]. For instance, R phase with small transformation strain (~1 %) can be confined by a percolated strain network with relatively low strength [46,48], whereas the B19′ phase

with much larger transformation strain (~10 %) necessitates a robust percolated strain network generated by cold-rolling in NiTi SMAs [25,26]. Consequently, R and B19′ phases may be sequentially confined in the same system within a given heterogeneous strain network. It is worth noting that the cold working and low-temperature annealing treatments utilized in this work may produce nanocrystalline structure with high-density defects [49,50]. Such nanocrystalline has also been observed to suppress B19′ phase while promote the intermediate R phase [51], contributing to the observed two-step transition behavior. The free-energy landscape under external loading to illustrate the transition pathway of B2→R→B19′ is shown in Fig. 5(e-f). Upon loading, the free-energy landscape tilt toward martensitic phases, yielding stress-induced transformation [52,53]. This two-step continuous transition pathway presents a minimal energy barrier, facilitating enhanced transformability with slim hysteresis, resulting in large recoverable strain, substantial ΔT_{ad}, and high COP_{mat}, while maintaining cyclic stability. This work provides a versatile approach to tailor the superelastic behavior of NiTi SMAs by simply using the traditional physical metallurgy trick, i.e., "beat and heat".

In conclusion, this study introduces a novel two-step continuous transition and unveils the associated cyclic-stable, low-fatigue superelastic functional properties in a $Ni_{50.8}Ti_{49.2}$ alloy subjected to 473 K annealing after a 40 % thickness reduction in cold rolling. This continuous and reversible pathway offers cyclic-stable superelasticity with a significant 5.9 % recoverable strain and a substantial 19.1 K elastocaloric ΔT_{ad}. The stress-induced B2→R→ B19′ continuous transition is directly evidenced by *in-situ* loading synchrotron-based HE-XRD. This unique transition pathway is facilitated by a specific heterogeneous nanoscale strain network. By leveraging the continuous transitions among different martensitic phases, this research could pave the way for enhancing the multifunctional performance and enabling a broader range of applications of SMAs.

CRediT authorship contribution statement

Qianglong Liang: Writing – original draft, Validation, Methodology, Investigation, Funding acquisition, Data curation, Conceptualization. **Dong Wang:** Methodology, Conceptualization. **Chuanxin Liang:** Visualization. **Xiangdong Ding:** Supervision, Funding acquisition. **Yunzhi Wang:** Writing – review & editing, Conceptualization.

Declaration of competing interest

The authors declare that they have no known competing financial interests or personal relationships that could have appeared to influence the work reported in this paper.

Acknowledgements

QL and XD acknowledge the support of the National Natural Science Foundation of China (Grants No. 52201228, and 51931004). QL also acknowledges the support of China Postdoctoral Science Foundation (No 2021M692514). DW would like to acknowledge the support from the National Key Research and Development Program of China (Grand No. 2021YFB3702603), the National Natural Science Foundation of China (Grants No. 52171012), the Fundamental Research Funds for the Central Universities (xhj032021015–06) and 111 project (BP2018008). YW acknowledges the support by the US National Science Foundation under Grant No. DMR-1923929, which has facilitated this international collaboration. Usage of the Advanced Photon Source for HE-XRD was kindly provided by Dr. Shilei Li and Dr. Yandong Wang of University of Science and Technology Beijing.

References

[1] M.O. McLinden, C.J. Seeton, A. Pearson, New refrigerants and system configurations for vapor-compression refrigeration, Science 370 (6518) (2020) 791–796.
[2] J. Dupont, P. Domanski, P. Lebrun, F. Ziegler, The role of refrigeration in the global economy, 38th note on refrigeration technologies (International Institute of Refrigeration, 2019) (2019).
[3] X. Moya, S. Kar-Narayan, N.D. Mathur, Caloric materials near ferroic phase transitions, Nat. Mater. 13 (5) (2014) 439–450.
[4] X. Moya, N.D. Mathur, Caloric materials for cooling and heating, Science 370 (6518) (2020) 797–803.
[5] S. Qian, Y. Geng, Y. Wang, J. Ling, Y. Hwang, R. Radermacher, I. Takeuchi, J. Cui, A review of elastocaloric cooling: materials, cycles and system integrations, Int. J. Refrig. 64 (2016) 1–19.
[6] L. Mañosa, A. Planes, Materials with Giant Mechanocaloric Effects: cooling by Strength, Adv. Mater. 29 (11) (2017) 1603607.
[7] I. Takeuchi, K. Sandeman, Solid-state cooling with caloric materials, Phys. Today 68 (12) (2015) 48–54.
[8] L. Ding, Y. Zhou, Y. Xu, P. Dang, X. Ding, J. Sun, T. Lookman, D. Xue, Learning from superelasticity data to search for Ti-Ni alloys with large elastocaloric effect, Acta Mater. 218 (2021) 117200.
[9] T. Simon, A. Kröger, C. Somsen, A. Dlouhy, G. Eggeler, On the multiplication of dislocations during martensitic transformations in NiTi shape memory alloys, Acta Mater. 58 (5) (2010) 1850–1860.
[10] J. Zhang, C. Somsen, T. Simon, X. Ding, S. Hou, S. Ren, X. Ren, G. Eggeler, K. Otsuka, J. Sun, Leaf-like dislocation substructures and the decrease of martensitic start temperatures: a new explanation for functional fatigue during thermally induced martensitic transformations in coarse-grained Ni-rich Ti–Ni shape memory alloys, Acta Mater. 60 (5) (2012) 1999–2006.
[11] D.M. Norfleet, P.M. Sarosi, S. Manchiraju, M.F.X. Wagner, M.D. Uchic, P. M. Anderson, M.J. Mills, Transformation-induced plasticity during pseudoelastic deformation in Ni–Ti microcrystals, Acta Mater. 57 (12) (2009) 3549–3561.
[12] A.N. Bucsek, L. Casalena, D.C. Pagan, P.P. Paul, Y. Chumlyakov, M.J. Mills, A. P. Stebner, Three-dimensional in situ characterization of phase transformation induced austenite grain refinement in nickel-titanium, Scr. Mater. 162 (2019) 361–366.
[13] Y. Gao, L. Casalena, M. Bowers, R. Noebe, M. Mills, Y. Wang, An origin of functional fatigue of shape memory alloys, Acta Mater. 126 (2017) 389–400.
[14] M.L. Bowers, Y. Gao, L. Yang, D.J. Gaydosh, M. De Graef, R.D. Noebe, Y. Wang, M. J. Mills, Austenite grain refinement during load-biased thermal cycling of a Ni49.9Ti50.1 shape memory alloy, Acta Mater. 91 (2015) 318–329.
[15] C. Chluba, W. Ge, R. Lima de Miranda, J. Strobel, L. Kienle, E. Quandt, M. Wuttig, Shape memory alloys. Ultralow-fatigue shape memory alloy films, Science 348 (6238) (2015) 1004–1007.
[16] Y. Song, X. Chen, V. Dabade, T.W. Shield, R.D. James, Enhanced reversibility and unusual microstructure of a phase-transforming material, Nature 502 (7469) (2013) 85–88.
[17] P. Hua, M. Xia, Y. Onuki, Q. Sun, Nanocomposite NiTi shape memory alloy with high strength and fatigue resistance, Nat. Nanotechnol 16 (4) (2021) 409–413.
[18] H. Chen, F. Xiao, X. Liang, Z. Li, X. Jin, T. Fukuda, Stable and large superelasticity and elastocaloric effect in nanocrystalline Ti-44Ni-5Cu-1Al (at %) alloy, Acta Mater. 158 (2018) 330–339.
[19] H. Chen, F. Xiao, X. Liang, Z. Li, Z. Li, X. Jin, N. Min, T. Fukuda, Improvement of the stability of superelasticity and elastocaloric effect of a Ni-rich Ti-Ni alloy by precipitation and grain refinement, Scr. Mater. 162 (2019) 230–234.
[20] P. Dang, F. Ye, Y. Zhou, L. Ding, J. Pang, L. Zhang, X. Ding, J. Sun, S. Dai, T. Lookman, D. Xue, Low-fatigue and large room-temperature elastocaloric effect in a bulk Ti49.2Ni40.8Cu10 alloy, Acta Mater. 229 (2022).
[21] D. Liang, Q. Wang, K. Chu, J. Chen, P. Hua, F. Ren, Q. Sun, Ultrahigh cycle fatigue of nanocrystalline NiTi tubes for elastocaloric cooling, Appl. Mater. Today 26 (2022) 101377.
[22] H. Lin, P. Hua, K. Huang, Q. Li, Q. Sun, Grain boundary and dislocation strengthening of nanocrystalline NiTi for stable elastocaloric cooling, Scr. Mater. 226 (2023) 115227.
[23] H. Hou, E. Simsek, T. Ma, N.S. Johnson, S. Qian, C. Cissé, D. Stasak, N. Al Hasan, L. Zhou, Y. Hwang, R. Radermacher, V.I. Levitas, M.J. Kramer, M.A. Zaeem, A. P. Stebner, R.T. Ott, J. Cui, I. Takeuchi, Fatigue-resistant high-performance elastocaloric materials made by additive manufacturing, Science 366 (6469) (2019) 1116–1121.
[24] X. Li, Q. Liang, T. Dong, C. Liang, D. Wang, Y. Wang, X. Ding, Fatigue-resistant elastocaloric effect in hypoeutectic TiNi58 alloy with heterogeneous microstructure, Acta Mater. 262 (2024) 119464.
[25] Q. Liang, S. Zhao, C. Liang, T. Zhao, D. Wang, X. Ding, S. Li, Y. Wang, Y. Zheng, X. Ren, M. Mills, Y. Wang, Strain states and unique properties in cold-rolled TiNi shape memory alloys, Acta Mater. (2022) 117890.
[26] Q. Liang, D. Wang, J. Zhang, Y. Ji, X. Ding, Y. Wang, X. Ren, Y. Wang, Novel B19′ strain glass with large recoverable strain, Phys. Rev. Mater. 1 (3) (2017) 033608.
[27] D. Wang, Q. Liang, S. Zhao, P. Zhao, T. Zhang, L. Cui, Y. Wang, Phase field simulation of martensitic transformation in pre-strained nanocomposite shape memory alloys, Acta Mater. 164 (2019) 99–109.
[28] D. Wang, Y. Ji, X. Ren, Y. Wang, Strain Glass State, Strain Glass Transition, and Controlled Strain Release, Annu. Rev. Mater. Res. 52 (1) (2022) 159–187.
[29] A. Ahadi, T. Kawasaki, S. Harjo, W.-S. Ko, Q. Sun, K. Tsuchiya, Reversible elastocaloric effect at ultra-low temperatures in nanocrystalline shape memory alloys, Acta Mater. 165 (2019) 109–117.

[30] Y. Yang, C. Liu, Y. Ji, L. He, X. Ren, Designed morphotropic relaxor boundary ceramic exhibiting large electrostrain and negligible hysteresis, Acta Mater. 208 (2021) 116720.
[31] Y. Yang, Y. Ji, M. Fang, Z. Zhou, L. Zhang, X. Ren, Morphotropic relaxor boundary in a relaxor system showing enhancement of electrostrain and dielectric permittivity, Phys. Rev. Lett. 123 (13) (2019) 137601.
[32] Y. Song, M. Jin, X. Han, X. Wang, P. Chen, X. Jin, Microstructural origin of ultrahigh damping capacity in Ni50.8Ti49.2 alloy containing nanodomains induced by insufficient annealing and low-temperature aging, Acta Mater. 205 (2021) 116541.
[33] M.J. Hÿtch, E. Snoeck, R. Kilaas, Quantitative measurement of displacement and strain fields from HREM micrographs, Ultramicroscopy 74 (3) (1998) 131–146.
[34] Y. Zheng, F. Jiang, L. Li, H. Yang, Y. Liu, Effect of ageing treatment on the transformation behaviour of Ti–50.9at.% Ni alloy, Acta Mater. 56 (4) (2008) 736–745.
[35] X. Moya, E. Defay, V. Heine, N.D. Mathur, Too cool to work, Nat. Phys. 11 (3) (2015) 202–205.
[36] J. Cui, Y. Wu, J. Muehlbauer, Y. Hwang, R. Radermacher, S. Fackler, M. Wuttig, I. Takeuchi, Demonstration of high efficiency elastocaloric cooling with large ΔT using NiTi wires, Appl. Phys. Lett. 101 (7) (2012).
[37] L. Porenta, P. Kabirifar, A. Žerovnik, M. Čebron, B. Žužek, M. Dolenec, M. Brojan, J. Tušek, Thin-walled Ni-Ti tubes under compression: ideal candidates for efficient and fatigue-resistant elastocaloric cooling, Appl. Mater. Today 20 (2020) 100712.
[38] J. Chen, K. Zhang, Q. Kan, H. Yin, Q. Sun, Ultra-high fatigue life of NiTi cylinders for compression-based elastocaloric cooling, Appl. Phys. Lett. 115 (9) (2019).
[39] J. Chen, C. Zhao, S. Zhang, W. Zhang, W. Liu, L. Lei, U. Ramamurty, G. Fang, Imparting high elastocaloric cooling potential to NiTi alloy by two-step enhancements, Mater. Sci. Eng., A 892 (2024) 146073.
[40] J. Chen, B. Liu, L. Xing, W. Liu, L. Lei, G. Fang, Toward tunable mechanical behavior and enhanced elastocaloric effect in NiTi alloy by gradient structure, Acta Mater. 226 (2022) 117609.
[41] J. Chen, L. Xing, G. Fang, L. Lei, W. Liu, Improved elastocaloric cooling performance in gradient-structured NiTi alloy processed by localized laser surface annealing, Acta Mater. 208 (2021) 116741.
[42] P. Dang, J. Pang, Y. Zhou, L. Ding, L. Zhang, X. Ding, T. Lookman, J. Sun, D. Xue, Improved stability of superelasticity and elastocaloric effect in Ti-Ni alloys by suppressing Lüders-like deformation under tensile load, J. Mater. Sci. Technol. 146 (2023) 154–167.
[43] L. Bumke, C. Zamponi, J. Jetter, E. Quandt, Cu-rich Ti52.8Ni22.2Cu22.5Co2.5 shape memory alloy films with ultra-low fatigue for elastocaloric applications, J. Appl. Phys. 127 (22) (2020).
[44] Y. Kim, M.-G. Jo, J.-W. Park, H.-K. Park, H.N. Han, Elastocaloric effect in polycrystalline Ni50Ti45.3V4.7 shape memory alloy, Scr. Mater. 144 (2018) 48–51.
[45] S. Hao, L. Cui, D. Jiang, X. Han, Y. Ren, J. Jiang, Y. Liu, Z. Liu, S. Mao, Y. Wang, Y. Li, X. Ren, X. Ding, S. Wang, C. Yu, X. Shi, M. Du, F. Yang, Y. Zheng, Z. Zhang, X. Li, D.E. Brown, J. Li, A transforming metal nanocomposite with large elastic strain, low modulus, and high strength, Science 339 (6124) (2013) 1191–1194.
[46] H. Zong, H. Wu, X. Tao, D. Xue, J. Sun, S.J. Pennycook, T. Min, Z. Zhang, X. Ding, Percolated strain networks and universal scaling properties of strain glasses, Phys. Rev. Lett. 123 (1) (2019) 015701.
[47] S. Sarkar, X. Ren, K. Otsuka, Evidence for strain glass in the ferroelastic-martensitic system Ti(50-x)Ni(50+x), Phys. Rev. Lett. 95 (20) (2005) 205702.
[48] D. Wang, D. Lv, Y. Gao, Y. Wang, X. Ren, Y. Wang, Defect strength and strain glass state in ferroelastic systems, J. Alloys Compd. 661 (2016) 100–109.
[49] J. Chen, L. Lei, G. Fang, Grain-size effects on the temperature-dependent elastocaloric cooling performance of polycrystalline NiTi alloy, J. Alloys Compd. 927 (2022) 166951.
[50] Z. Deng, K. Huang, H. Yin, Q. Sun, Temperature-dependent mechanical properties and elastocaloric effects of multiphase nanocrystalline NiTi alloys, J. Alloys Compd. 938 (2023) 168547.
[51] T. Waitz, V. Kazykhanov, H.P. Karnthaler, Martensitic phase transformations in nanocrystalline NiTi studied by TEM, Acta Mater. 52 (1) (2004) 137–147.
[52] D. Wang, Y. Wang, Z. Zhang, X. Ren, Modeling abnormal strain states in ferroelastic systems: the role of point defects, Phys. Rev. Lett. 105 (20) (2010) 205702.
[53] D. Wang, S. Hou, Y. Wang, X. Ding, S. Ren, X. Ren, Y. Wang, Superelasticity of slim hysteresis over a wide temperature range by nanodomains of martensite, Acta Mater. 66 (2014) 349–359.